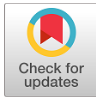

Research Article | Vol. 27, No. 4 | 18 Feb 2019 | OPTICS EXPRESS 5729

Optics EXPRESS

Investigation of laser annealing mechanisms in thin film coatings by photothermal microscopy

FACUNDO ZALDIVAR ESCOLA,[1,*] NÉLIDA MINGOLO,[1] OSCAR E. MARTÍNEZ,[1,2] JORGE J. ROCCA,[3] AND CARMEN S. MENONI[3]

[1]*Departamento de Física, Facultad de Ingeniería, UBA, Av. Paseo Colón 850, C1063ACV, Buenos Aires, Argentina*
[2]*Consejo Nacional de Investigaciones Científicas y Técnicas (CONICET), Argentina*
[3]*Department of Electrical and Computer Engineering, Colorado State University, Fort Collins, CO 80523, USA*
**facundozaldivar@gmail.com*

Abstract: We study the evolution of the absorptance of amorphous metal oxide thin films when exposed to intense CW laser radiation measured using a photothermal microscope. The evolution of the absorptance is characterized by a nonexponential decay. Different models that incorporate linear and nonlinear absorption, free carrier absorption, and defect diffusion are used to fit the results, with constraints imposed on the fit parameters to scale with power and intensity. The model that best fits is that two types of interband defects are passivated independently, one by a one-photon process and the other one by a two-photon process.

© 2019 Optical Society of America under the terms of the OSA Open Access Publishing Agreement

1. Introduction

One of the challenges in engineering multilayer dielectric interference coatings (IC) for near infrared high-energy lasers is to create structures that perform consistently under intense laser illumination, showing no signs of discoloration or catastrophic failure. The failure mechanisms in the IC's may be of different origin depending on the duration of the laser pulse. Interference coatings typically consist of stacks of two amorphous alternating materials, which have the largest variation in refractive index and the minimum extinction at the laser wavelength. The amorphous thin films are deposited by physical vapor deposition onto transparent substrates. Inherently, These nearly stoichiometric amorphous layers contained a family of interband point defects that affect their absorption and play a role in the coating's damage under illumination [1,2]. Shallow level defects are known to contribute to absorption at 1064 nm. Markosyan et al [3] showed that the 1064 nm absorption loss of Ta_2O_5 thin films can be altered with simultaneous illumination at shorter wavelengths, an indication of the activation of electronic defects [3]. Langston et al [4], showed the deposition conditions affect the density of structural point defects in Sc_2O_3 that were identified as oxygen interstitials [4]. Post-treatment, such as annealing and laser conditioning reduces the density of interband electronic states [5]. Moreover, the annealing out of structural defects has also been attributed to improvements on the laser damage performance of thin films when exposed to near infrared nanosecond pulses [6,7]. It was argued that these improvements result from passivating interband electronic states by laser conditioning [7].

In this work, we study the evolution of the absorptance of amorphous metal oxide thin films, and show a permanent reduction. The evolution of the absorptance at 1064 nm, measured using a photothermal microscope, is characterized by a nonexponential decay. Different models that incorporate linear and nonlinear absorption, free carrier absorption and defect diffusion, are used to fit the results, with constraints imposed on the fit parameters to scale with power and intensity. The model that best fits the behavior of the absorptance is one

#354651 https://doi.org/10.1364/OE.27.005729
Journal © 2019 Received 5 Dec 2018; revised 26 Jan 2019; accepted 30 Jan 2019; published 14 Feb 2019

in which two types of interband defects are passivated independently, one by a one photon process and the other by a two photon process.

The results of our analysis support previous findings and analysis of laser annealing in HfO_2/SiO_2 and ZrO_2/SiO_2 with nanosecond pulses [7]. They are more rigorous in that they identify a dominant mechanism for the passivation of shallow interband electronic states. The fact that the reduction in absorptance in Sc_2O_3-SiO_2 stacks is permanent indicates complete passivation.

2. Experimental

2.1 Setup

The photothermal microscope used in this work is a modification of the focus error thermal lens technique previously demonstrated [8,9]. Figure 1 shows a diagram of the experimental setup. A 20W fiber coupled IPG Photonics laser model YLR-20-1064-LP with TTL current modulation was used as the pump laser. The laser delivers up to 6.7 W (average power) on the sample after losses in the optical system and 50% loss due to modulation are accounted for. A 13 mW collimated He:Ne laser was used as the probe beam. The pump beam was used to heat the sample for the absorptance measurement and was also responsible for the thin film annealing.

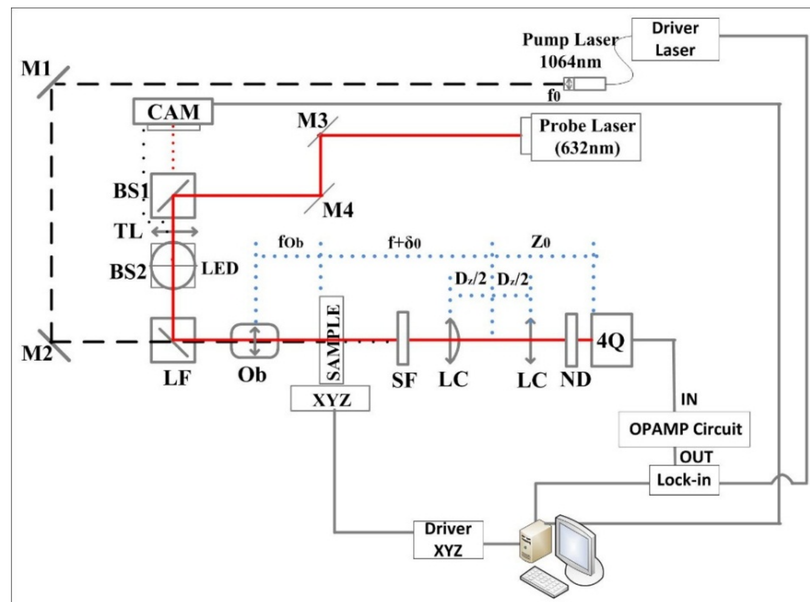

Fig. 1. Schematics of the photothermal microscope. M1 and M2: 1064nm-mirrors. M3 and M4: HeNe-mirrors. LF: long pass filter (cutoff 750nm). SF: short pass filter (cuttof 850nm). f_0 collimator lens (pump beam). Ob: objective lens (f_{Ob} = 10mm). BS1: beam splitter (R: 90% probe reflectivity). BS2: beam splitter (R: 50% probe reflectivity) TL: tube lens (f_{TL} = 200mm, focuses the probe beam onto the back focal plane of the objective). LC: cylindrical lenses (f = 75mm). D_z, Z_0 and δ_0: distances of the focus measurement system. XYZ: Micrometric translation stage. ND: neutral filters. LED: Lighting. CAM: Camera. 4Q: Four-Quadrant detector.

Collimating lens (f_0) directs the pump beam towards two 1064nm-mirrors (M1 and M2) and reaches the sample passing through a long pass filter (LF: cutoff 750nm) and the objective lens (Ob: focal distance f_{Ob} = 10mm). These two lenses (f_0 and objective) configure a telescope that focuses the pump beam to a beam radius to σ_{pump} = 1µm on the sample (we define σ as the beam radius i.e. ½ the beam waist). The probe beam is reflected in two mirrors M3 and M4 and the beam splitter BS1 (90% probe reflectivity). The tube lens (TL, focal

Optics EXPRESS

distance f_{TL} = 200mm) focuses the probe beam onto the back focal plane (BFP) of the objective, after being reflected on the long pass filter (LF) in such a way that it is collimated at the sample surface with a size σ_{probe} = 11.5µm.

The focused pump beam is partially absorbed by the sample surface and the collimated probe beam passes through the substrate. Two identical cylindrical lenses (CL: focal length f = 75mm), whose axes are perpendicular to each other, are placed on the optical axis separated by a distance D_z introducing astigmatism in the probe beam. Due to the thermal lensing effect the probe beam focus position at the Four-Quadrant detector (4Q) position changes at the pump modulation frequency. An operational amplifier based circuit (OPAMP) builds the unbalance signal (C1 + C3)-(C2 + C4), where the quadrants of the 4Q have been denoted as C1, C2, C3 and C4 in the clockwise direction. We use a lock-in amplifier (Stanford Sr810) to detect the component of this signal at the pump modulation frequency. The circuit also generates the sum signal C1 + C2 + C3 + C4 (Signal SUM).

A short pass filter (SF: cutoff 850nm) was located before the detector in order to prevent unwanted contributions from the pump beam and neutral density (ND) filters were used to attenuate the power of the probe beam depending on the sample transmission to avoid saturating the four-quadrant detector.

The alignment procedure and focusing of the pump beam over the sample were simplified by using a camera added to the experimental setup. The objective plus the tube lens (TL) configures also a telescope that images the sample surface onto the camera. A beam splitter (BS1) allows part of the reflected beams to reach the camera. A second beam splitter (BS2: Transmission 50%, Reflection 50%)) was used to allow illumination of the sample with a LED source.

The surface of the sample is positioned at the focal plane of the pump beam and swept by means of a micrometric translation stage (XYZ). The focal spot size of the pump beam defines the lateral resolution of the system. The size of the probe beam defines the pump beam modulation frequency (f_{pump}), since it is chosen to equate the beam size to the diffusion distance (µ) of the thermal wave generated by the modulated pump beam inside the substrate. In this way, the chosen frequency corresponds to the time necessary for the heat to diffuse a distance of the order of the size of the probe beam in the sample. . The contribution to the signal from the material is proportional to the temperature dependence of the refractive index dn/dT and the length of the heat-affected zone. Hence, in order to neglect the film's contribution to the signal and have a common calibration for all samples, the probe beam diameter should be selected much larger than the film thickness. The film affects the calibration by a factor defined by

$$\frac{\frac{dn_{film}}{dT} l_{film}}{\frac{dn_{substrate}}{dT} \mu} \tag{1}$$

Therefore, by selecting a probe beam diameter much larger than the film thickness, the path of the probe beam through the heat affected zone is dominated by the path through the substrate. As the probe beam diameter was selected much larger than the thin film thickness, the material properties relevant to the determination of the signal are the film absorptance and the substrate thermal and optical properties. This fact will allow the calibration of the signal in absorptance units irrespective of the film material. For fused silica, the thermal diffusivity is D = 0.008cm^2/s, therefore:

$$\mu = \sqrt{\frac{D}{\pi f}} = \sigma_{probe} \Rightarrow f_{pump} = \frac{D}{\pi \sigma_{probe}^2} \simeq 1.7KHz \tag{2}$$

With the above considerations, the focus error signal FE at the modulation frequency of the pump beam is expressed as:

$$FE\big|_{f_{pump}} = \frac{\left[(C1+C3)\text{-}(C2+C4)\right]\big|_{f_{pump}}}{C1+C2+C3+C4}\frac{1}{<P_{pump}>} = \frac{\text{Signal Amplitude (V)}}{<P_{pump}(W)>\ \text{Signal Sum (V)}} \quad (3)$$

Calibration of the photothermal microscope was carried out using samples whose absorption was known. The calibration samples are deposited also by ion beam sputtering. The PCI is calibrated using a sample with high absorptance that can be determined from spectrophotometry data or by fitting the transmission curve vs wavelength with a program like Optilayer and using zero as the second point to draw a straight line for detector voltage signal vs loss.

The mean value of the signal obtained along spatial scans of 50μmx50μm and a step of 5μm was compared with the absorptance value of the same sample obtained by the PCI technique [8]. This process was carried out in two zones of the five samples, taking as uncertainty of the measurement the standard deviation of these values in each map. This uncertainty corresponds to the inhomogeneity of the sample and not to fluctuations of the technique. The calibration curve is presented in Fig. 2.

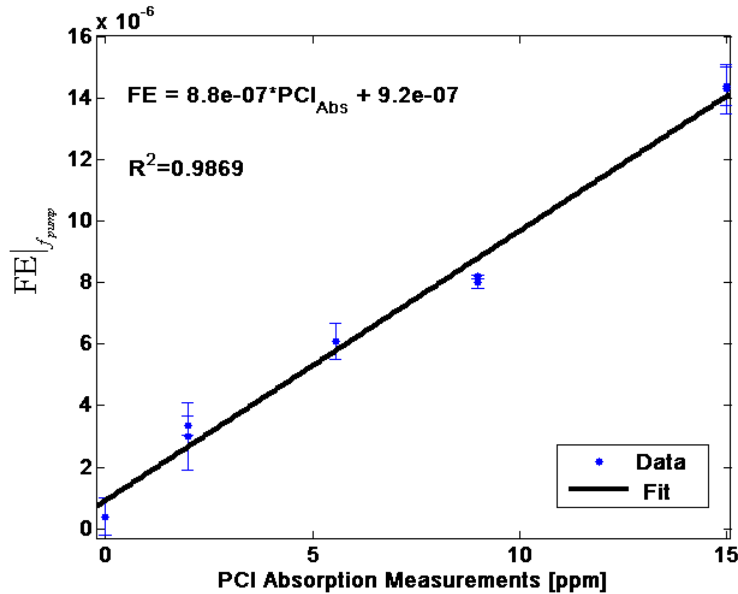

Fig. 2. Calibration of the FE signal against the absorption loss of the samples measured by Photothermal Common Path Interferometry (PCI).

For all cases the modulation frequency was 1650Hz, the lock-in amplifier integration time was 100ms, and the time between measurements was 1s. The probe beam size was σ_{Probe} = 11.5μm and the minimum pump beam diameter was σ_{Pump} = 1.0μm. The pump beam size was measured imaging the beam reflected on the substrate onto a camera previously calibrated and checked for linearity. The image was fit by a Gaussian. The probe beam was larger and could be measured by scanning a sharp knife edge. The maximum pump power was 6.7W, which yielded a maximum pump intensity of 0.23GW/cm^2.

To demonstrate the sensitivity of the photothermal microscope and the permanent reduction in the absorptance due to laser irradiation we used a SiO_2 film deposited on a fused silica substrate with an average absorptance of 5ppm. The measurement consisted of determining focus error signal maps subsequently converted to absorptance using the calibration of Fig. 2. To reject spurious peaks from the signal and reduce the noise the same area was repeatedly measured and averaged pixel by pixel. A first repeated scan on a 40μm by 40μm region was performed (not shown) and a day later a larger region including the

previously scanned one was measured (Fig. 3(a)). In this larger scan, the reduction in absorptance in the previously scanned region is evident, confirming the permanent nature of the changes induced in the absorptance. In Fig. 3(b) the average absorptance over 22 pixels as a function of time is presented showing the laser induced annealing phenomenon. Notice that this microscope is capable of identify changes in absorptance as small as 0.5 ppm.

The temperature rise due to the absorption of the pump beam can be estimated from the model for a modulated Gaussian pump presented in [10] yielding a temperature rise at the beam center of about 10K. Hence, a temperature annealing mechanism can be discarded as an explanation of the observed decay in the absorptance since typically thermal annealing is performed during about 10 hours at 300C.

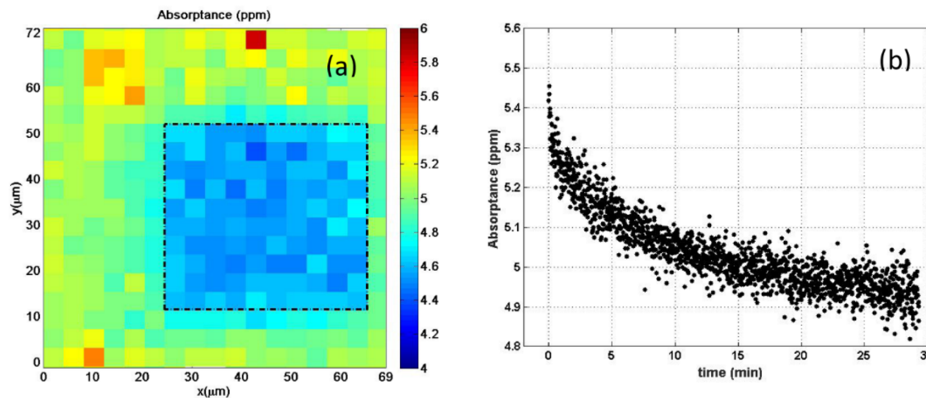

Fig. 3. (a) Absorptance map for a SiO_2 film deposited on a fused silica substrate. The dashed lines delimit the initial sweep of 40µm by 40µm. (b) Average absorptance over 22 pixels as a function of time. The pixel size is 4 µm. The change in absorptance due to laser annealing is 0.5 ppm.

2.2 Samples

For the annealing study, a multilayer stack designed as an antireflection coating for 1064 nm deposited onto a UV fused silica substrate was used. This sample consisted of two layers of SiO_2 intercalated with two layers of Sc_2O_3. The first layer, in contact with the substrate, Sc_2O_3, has a thickness of 50nm. It is followed by a 400 nm thick SiO_2 layer, then a 180 nm Sc_2O_3 layer and finally a 160 nm SiO_2 layer. This sample was deposited by reactive ion beam sputtering. During the deposition of Sc2O3 from a metal target the oxygen flow was selected to obtain a film with an absorption loss of ~50 ppm [4]. The SiO_2 instead was deposited from an oxide target, which typically results in an amorphous thin film with an absorption loss of a few parts per million at 1064 nm.

For this case the Sc_2O_3 total thickness was 230nm, 50 times smaller than the probe beam radius, which guarantees that the neglected correction factor due to the film contribution to the signal given in Eq. (1) is satisfactory.

The average absorptance of this sample at 1064 nm was 113 ppm. Two different pump beam diameters and different powers were used. For each set, the time evolution of the absorptance was obtained. Table 1 summarizes the beam power, area, and the number of points measured on the different runs. The measured average absorptance as a function of time for each condition is presented in Fig. 4. The variations in the absorptance are of the order of 10 ppm. The time evolution of both the SiO_2 shown in Fig. 3 and the SiO_2-Sc_2O_3 multilayer of Fig. 4 cannot be characterized by a single exponential decay and will be analyzed in terms of different models. Again, the direct thermal annealing mechanism is discarded as the temperature rise (around 200K for the highest pump intensity) and the time

span of this study are below the values for thermal annealing treatments used for this type of samples.

Table 1. Data for the different sets of measurements.

Series name	Power (mW)	Beam area (μm^2)	Number of averages
A1	6740	5.9	32
A2	5200	5.9	18
A3	3660	5.9	6
B1	4430	2.95	29
B2	1997	2.95	10
B3	996	2.95	27

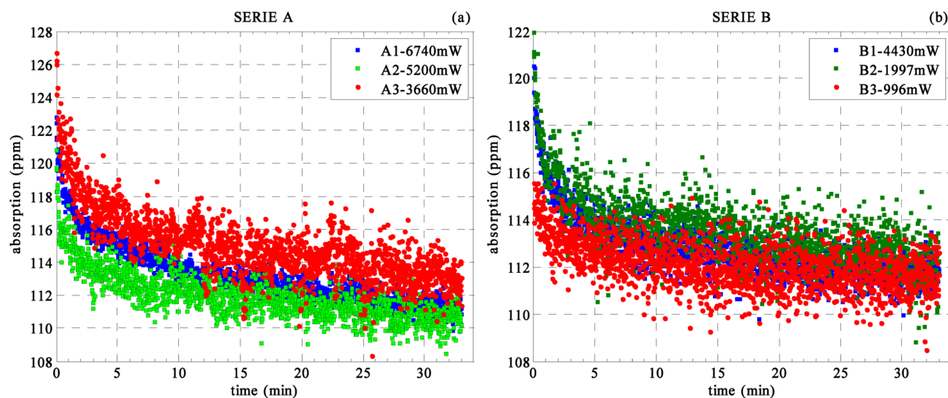

Fig. 4. Absorptance decay for the six cases of Table 2 as a function of time showing that the annealing process is characterized by an apparent fast process in the first minute followed by a slower process of tens of minutes.

In order to test if water adsorbed on the surface could have any influence in the observed evolution of the absorptance behavior shown in Fig. 4, the experiments were repeated flowing dry Argon. No detectable difference was encountered.

3. Models

Several models were used to fit the absorptance decay of Fig. 4 and gain insight on the annealing mechanisms. The antireflection coating design used for this study yields an electric field distribution essentially uniform across the coating, and hence the absorption can be in any layer or at the interface. Absorption from the SiO_2 layers can be discarded as it was shown before that these layers have only around 5ppm absorptance.

In Fig. 5 a schematic description of the possible mechanisms to be analyzed is drawn. Shallow native defects absorbing at around $\lambda = 1\mu m$ and $\lambda = 500nm$ [4] are probably related to oxygen interstitials as the absorption increases with increased O_2 partial pressure [11]. We assume transitions to the conduction band by one photon absorption from the shallowest state and two photon absorption from the second state. Electrons in the conduction band can absorb photons relaxing within the band by collisions with the lattice vibrations, heating the film. Multiphoton excitations from deeper states are included. The relaxation of the electrons to a deep trap state, depleting the electrons from the shallow states and hence reducing the absorptance is also considered. Diffusion of defects within the heated region, not included in the schematics of Fig. 5, is also discussed.

The pump intensity in our experiments was as high as 0.23 GW/cm^2, a high value for CW irradiation without damage. Hence, the experiments were probably carried out very close to the damage threshold of Sc_2O_3. At such high intensities, free carrier absorption in the conduction band becomes important and was therefore included in the models. One possibility was to assume that the local heating gives rise to diffusion of the defects until

Optics EXPRESS

annealed by collision with other type of defects. The other possibility is that the defects simply anneal by the temperature rise. As direct absorption from shallow states cannot heat the material to high enough temperature [12], a significant temperature rise, if present, must be originated in free carrier absorption. Other options are multiphoton absorption from deeper lying interband states, and combination of several of the mentioned mechanisms. The reduction in the absorptance can be explained by the annealing out of the shallow defects or the capture of the electrons by deep lying interband states.

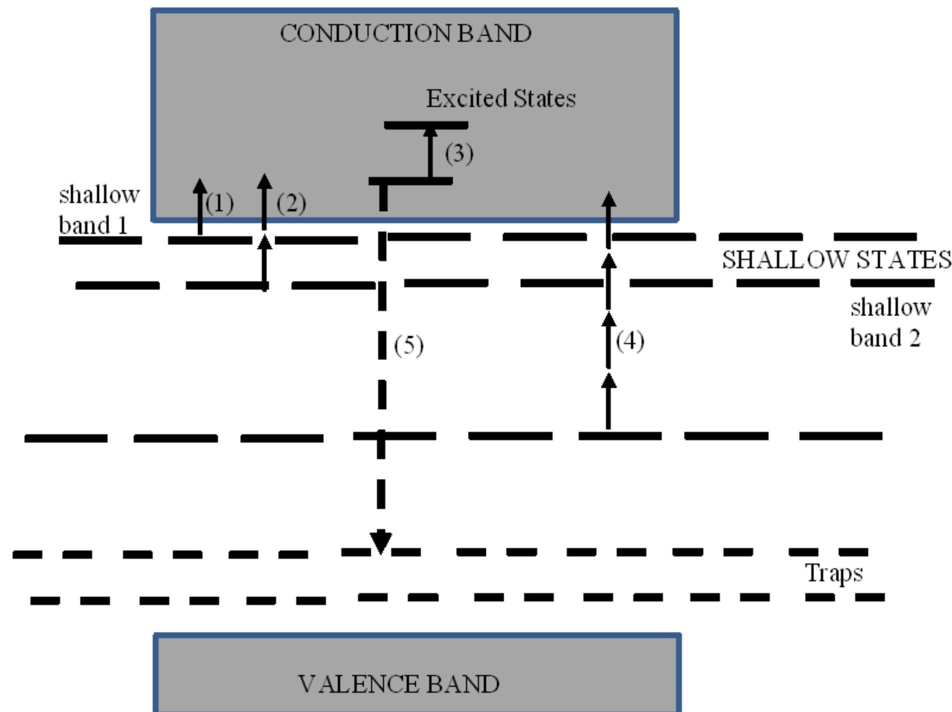

Fig. 5. Schematics of a typical band diagram of an oxide showing the different mechanisms used to analyze the absorptance recovery. (1) One photon absorption from a shalow state. (2) Two photon absorption from a deeper shallow state. (3) Free electron intraband absorption in the conduction band. (4) n photon absorption from a deep trap state. (5) Decay to a deep trap state. Not indicated are defect annihilation by temperature or collision. In the case of Sc_2O_3 the bandgap is 5.7eV.

For each measurement made at different pump powers and pump beam sizes the data were fitted and the quality of the fit, which was limited by the noise of the measurement, was evaluated based on the consistency of the trends and dependences of the model parameters with the pump power and beam size. This allowed us to select the possible mechanism responsible for the laser annealing among the different proposals tried. The expected analytical dependence of the absorptance decay and pump beam parameters for all different models is derived next.

3.1 Stretched exponential relaxation (SER)

Since the seminal paper by Kohlrausch in 1854 [13] many systems have been shown to relax following a common equation given by:

$$c(t) = c(0)\exp\left(-\left(\frac{t}{\tau}\right)^{\beta}\right) \tag{4}$$

where c is a concentration and β is a stretching factor between 0 and 1. In particular, Devine [14] has shown that the annealing of defects in amorphous SiO_2 follows such law. This behavior has been found in more than 70 different systems as diverse as glasses, polymers and spin glasses, and have been explained as due to the presence of traps frozen in the amorphous matrix that capture excitations that diffuse freely within an otherwise homogeneous medium [15–17]. This trapping process annihilates the defects depleting their concentration. This model provides a value for the stretching parameter:

$$\beta = \frac{d}{d+2} \tag{5}$$

where d is the effective dimension for the diffusion within the matrix and is expected to be between 1 and 3. For d = 3 the value β = 3/5 is expected, that would drop to β = 1/3 for d = 1.

If a SER process were responsible for the laser induced annealing observed in the deposited dielectric thin films one would expect that the rate coefficient 1/τ to be proportional to the beam intensity and the stretching parameter β to be constant at least within a single sample.

3.2 Multiphoton defect annealing

For this laser induced annealing model, we assume that the defect concentration evolves following locally an exponential decay as:

$$\frac{C(x,y,t)}{C_0(x,y)} = \exp(-\frac{t}{\tau}) \tag{6}$$

where the rate 1/τ accounts for the laser induced reaction and hence changes from site to site following a power law that depends on the number of photons simultaneously absorbed for the transition to take place

$$\frac{1}{\tau} = aI^n\left(x,y\right) = aI_0^n \exp(-(\frac{n\rho^2}{2})) = \frac{1}{\tau_0}\exp(-(\frac{n\rho^2}{2})) \tag{7}$$

where a Gaussian beam profile has been assumed, $\rho^2 = (x^2+y^2)/\sigma_{pump}^2$ and σ_{pump} is the beam radius. Notice that $1/\tau_0$ is proportional to the nth power of the peak intensity I_0.

The photothermal signal is proportional to the absorbed power that results from the overlap integral of the incident beam intensity with the remaining defect concentration:

$$S \propto \iint \exp\left(-\left(\frac{\rho^2}{2}\right)\right)\exp(-\frac{t}{\tau})\rho d\rho d\varphi \tag{8}$$

Changing variables as

$$g = \exp\left(-\left(\frac{\rho^2}{2}\right)\right) \tag{9}$$

and

$$t^{'} = \frac{t}{\tau_0} \tag{10}$$

It results in

$$S \propto \int_0^1 \exp(-(g^n t'))dg = \frac{\Gamma\left(\frac{1}{n}\right) - \Gamma\left(\frac{1}{n}, t'\right)}{n t^{1/n}} \tag{11}$$

where Γ is the incomplete gamma function. For the special case of single photon transitions n = 1 and

$$S \propto \frac{(1-\exp(-t'))}{t'} \tag{12}$$

For a two photon transition, n = 2 and

$$S \propto \frac{\sqrt{\pi} erf\left(\sqrt{t'}\right)}{2\sqrt{t'}} \tag{13}$$

Values n>2 are less likely to occur due to the low cross sections for multiphoton processes [18] but we included them in the fit because as it will be shown a higher n gives rise to better fits of the temporal behavior of the experimental results indicating the convenience of including these mechanisms for completeness.

3.3 One type of defect excited by one or two photons

In this case, the excitation rate has two terms:

$$\frac{1}{\tau} = a_1 I_0 \exp(-(\frac{\rho^2}{2})) + a_2 I_0^2 \exp(-(\frac{2\rho^2}{2})) \tag{14}$$

and the signal results

$$S \propto \int_0^1 \exp[-(t(b_1 g + b_2 g^2))]dg = \frac{\sqrt{\pi}\exp\left(\frac{c_1^2 t}{4}\right)\left[erf\left(\frac{\sqrt{t}(c_1+2c_2)}{2}\right) - erf\left(\frac{c_1\sqrt{t}}{2}\right)\right]}{2c_2\sqrt{t}} \tag{15}$$

where b_1 is proportional to the intensity and b_2 to the intensity squared, and $c_1 = b_1 / \sqrt{b_2}$ and $c_2 = \sqrt{b_2}$.

One particular case for this mechanism is shallow state absorption followed by intraband free carrier absorption. Assuming the occupied shallow state initial density is N_0 and N is the free carrier concentration, then (N_0-N) is the steady state occupied shallow state density. In this case, the absorptance (α) is proportional to:

$$\alpha = a\left(N_0 - N\right) + bN = \left[\frac{a}{1+\sigma I \tau} + \frac{b}{1+\frac{1}{\sigma I \tau}}\right] N_0 \approx (a + b\sigma I \tau) N_0 \tag{16}$$

where σ is the shallow state absorption cross section, I the pump intensity and τ the decay time from the conduction band back to the shallow state. The approximate solution for unsaturated transitions (low power) predicts an absorption coefficient that varies linearly with intensity as:

$$\alpha I = a N_0 I + b\sigma N_0 \tau I^2 \tag{17}$$

Optics EXPRESS

as found in this case of combined one photon and two photon mechanism of Eq. (14).

3.4 Two types of defects excited independently by one or two photons

This is simply a linear combination of the single defect situation presented in 3.2. Three cases will be analyzed: a- both defects anneal by the action of a single photon mechanism, b- one defect is annealed by a one photon mechanism and the other one by a two photon mechanism, c- both defects are annealed independently by two photon mechanisms.

4. Fits and discussion

The results were fitted using the Trust-Region Method for Nonlinear Minimization of the least absolute residual (LAR) (uncertainties presented are the 95% confidence bounds) with the models described in section 3 and combinations of two of them. For each case, we show one fit and a table of the fitted parameters with confidence intervals for the entire set of measurements. The parameters from the fits for each model are contrasted with the expected dependences with pump intensity as discussed in section 3.

4.1 Stretched exponential relaxation (SER)

Figure 6 shows the result of the fit using SER. The parameters obtained from the fit are summarized in Table 2. The expression used for the fit is:

$$f(t) = a \exp\left(-\left(\frac{t}{\tau}\right)^{\beta}\right) + c \tag{18}$$

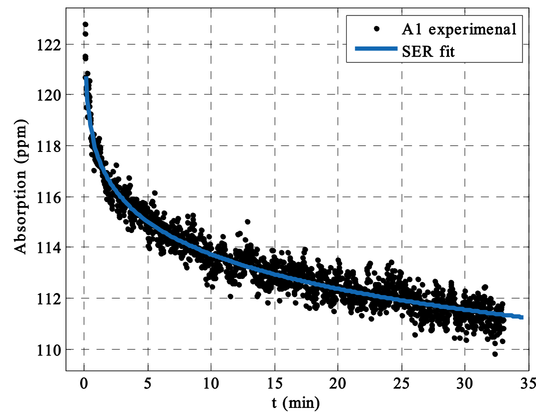

Fig. 6. Fit with the expression for stretched exponential relaxation using Kohlrausch's expression (Eq. (18)).

From the model one should expect that the time constant τ be inversely proportional to the power and that β (that depends on the dimension) remain constant. The drastic reduction of β with decreasing power is inconsistent with the assumptions and despite the power dependence of τ is not conclusive (due to the large uncertainties from the fit) this mechanism can be ruled out as responsible for the annealing.

Table 2. Parameters obtained for the fit using Kohlrausch's expression (Eq. (18)). The values in the parenthesis are the confidence interval (95%).

sample	a (ppm)	τ (min)	β	c (ppm)	R^2
A1	10 (9.3, 10.7)	8.141 (7.4, 8.9)	0.5589 (0.51, 0.62)	110.4 (110, 110.8)	0.93
A2	20(−0.15, 40.2)	9.3 (−13.7, 32.3)	0.1738 (−0.005, 0.35)	105 (95, 115)	0.73
A3	67 (−51, 185)	22 (−150, 194)	0.076 (−0.06, 0.21)	89 (32, 147)	0.96
B1	20 (18, 22)	0.50 (0.33, 0.68)	0.19 (0.17, 0.21)	109.6 (109.3, 110)	0.99

4.2 n photons process

In this case we assume a single type of defect that is annealed by the simultaneous absorption of n photons. In Fig. 7 the fit for n = 1, 2, 3, 4, and 10 are shown for one example (a detail for short times is presented in Fig. 7(b). As mentioned before the high n's were included because reproduce better the short time behavior of the measured data. In Table 3 the retrieved time constant and R^2 of the fit are presented.

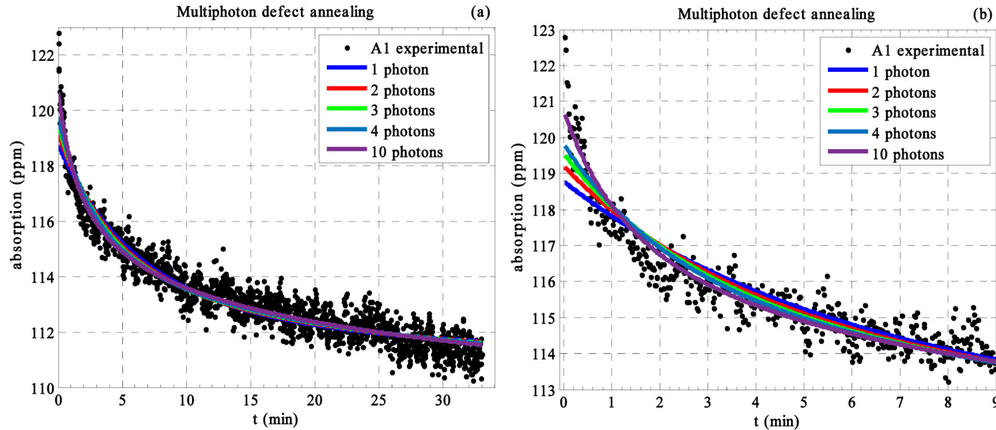

Fig. 7. Fit for measurement A1 with 1, 2, 3, 4 and 10 photon processes. a) Full measurement. b) Zoom out of the short time evolution.

Table 3. Multiphoton process. Parameter $1/\tau_0$, n: number of photons simultaneously absorbed. In parenthesis the 95% confidence interval.

Set		n = 1	n = 2	n = 3	n = 4	n = 10
A1	$\frac{1}{\tau_0}$ (min-1)	0.2024 (0.1995, 0.2053)	0.4143 (0.389, 0.4396)	0.5745 (0.5335, 0.6155)	0.7381 (0.6786, 0.7977)	1.639 (1.437, 1.842)
	R^2	0.9941	0.9175	0.9217	0.9245	0.9314
A2	$\frac{1}{\tau_0}$ (min-1)	0.2479 (0.2368, 0.2589	0.6066 (0.5256, 0.6875)	0.703 (0.6575, 0.7486)	0.9513 (0.8078, 1.095)	9.889 (4.34, 15.44)
	R^2	0.9493	0.7045	0.9533	0.8147	0.725
A3	$\frac{1}{\tau_0}$ (min-1)	0.2958 (0.2879, 0.3036)	0.6974 (0.6094, 0.7853)	0.921 (0.8914, 0.9506)	1.455 (1.176, 1.735)	3.621 (2.349, 4.892)
	R^2	0.9803	0.7308	0.989	0.7401	0.7458

The fit appears to improve for short times as the number of photons increases but the retrieved parameters are inconsistent (see Table 4). In fact, the parameter $1/\tau_0$ in Eq. (7) should scale with the nth power of the intensity and conversely it decreases with power. This inconsistency rules out any single n photon process.

4.3 Single type of defect annealed by one and two photons

As discussed in section 3.3 two rate parameters appear in this process, b_1 and b_2, that should scale with the intensity and the intensity squared respectively. The equation used for the fit (from Eq. (15)) is:

$$S = a\frac{\sqrt{\pi}\exp\left(\frac{c_1^2 t}{4}\right)\left[erf\left(\frac{\sqrt{t}(c_1+2c_2)}{2}\right) - erf\left(\frac{c_1\sqrt{t}}{2}\right)\right]}{2c_2\sqrt{t}} + c \qquad (19)$$

A single fit is shown in Fig. 8

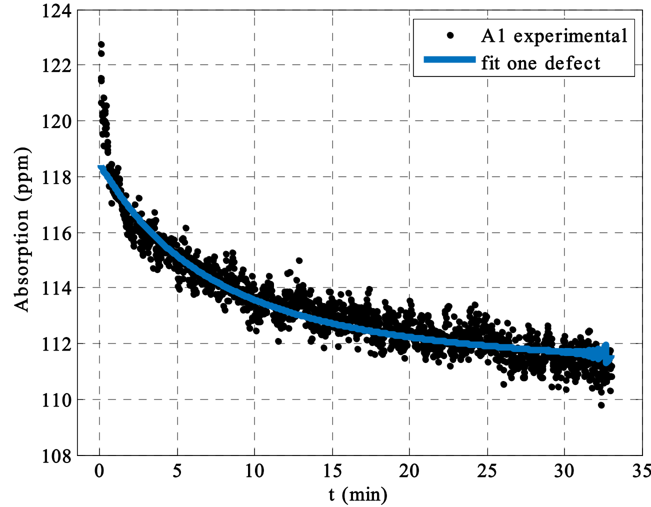

Fig. 8. Fit of the absorptance decay for sample A1 for one type of defect with an excitation process that includes a combination of one and two photons absorbed. The fit is not adequate for short times.

Table 4. Fitted parameters for the one and two photon annealing model for a single defect. In parenthesis the 95% confidence interval. Fitted function: Eq. (19)

sample	c_1 ($min^{-1/2}$)	c_2 ($min^{-1/2}$)	R^2
A1	1.02 (1.02, 1.02)	0.1143 (0.111, 0.118)	0.95
A2	0.7895 (0.7821, 0.7969)	0.1564 (0.1497, 0.1632)	0.95
A3	0.9971 (0.9971, 0.9971)	0.1731 (0.1668, 0.1794)	0.96

From the model one would expect c_1 to remain constant with the intensity because b_1 scales linearly and b_2 quadratically with intensity. This is consistent with the measurements and fits. But c_2 decreases when it should scale linearly with the intensity. This inconsistency rules out this mechanism.

4.4 Two type of defects

In this case we assume that there are two type of defects with different and independent concentrations that anneal both by a one photon mechanism (M_1 + 1) or one by a one photon mechanism and the other one by a two photon mechanism (M_1 + 2) or that both defects anneal by a two photon mechanism (M_2 + 2). For the three processes, one particular fit is shown in Fig. 9 and the parameters are listed in Table 5 for M_1 + 1, Table 6 for M_1 + 2 and Table 7 for M_2 + 2. The equations for the fit are a combination of Eq. (11) and result for M_1 + 1

$$\mathrm{Sfit} = a_1\frac{(1-\exp(-b_1 t))}{(b_1 t)} + a_2\frac{(1-\exp(-b_2 t))}{(b_2 t)} + c \qquad (20)$$

and for M_1 + 2

Optics EXPRESS

$$\mathrm{Sfit} = a_1 \frac{(1-\exp(-b_1 t))}{(b_1 t)} + a_2 \frac{\Gamma(0.5) - \Gamma(0.5, b_2 t)}{\mathrm{sqrt}(b_2 t)} + c \tag{21}$$

and finally for M_2 + 2:

$$\mathrm{Sfit} = a_1 \frac{\Gamma(0.5) - \Gamma(0.5, b_1 t)}{\mathrm{sqrt}(b_1 t)} + a_2 \frac{\Gamma(0.5) - \Gamma(0.5, b_2 t)}{\mathrm{sqrt}(b_2 t)} + c \tag{22}$$

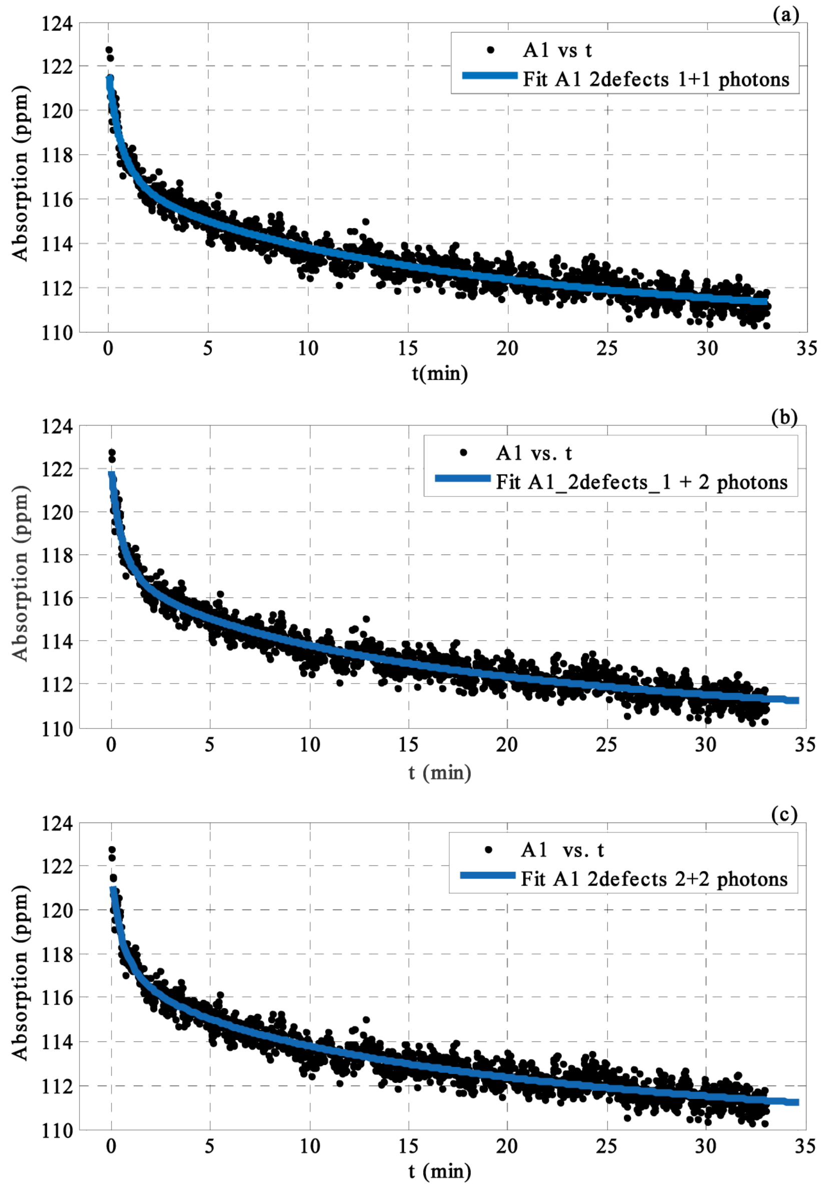

Fig. 9. a) Two types of defects that anneal each by a one photon mechanism: (M_1 + 1). b) Two type of defects that anneal one by a one photon process and the other one by a two photon process (M_1 + 2). c) Two type of defects that anneal each by a two photon process (M_2 + 2)

Optics EXPRESS

Table 5. Rate parameters for a two defects one photon annealing (M_1 + 1). In parenthesis the 95% confidence interval. Fit with Eq. (20)

M_1 + 1	b_1 (1/min)	b_2 (1/min)	R^2
A1	2.724 (2.268, 3.181)	0.08982 (0.07663, 0.103)	0.9393
A2	1.943 (1.365, 2.52)	0.04139 (0.008593, 0.07418)	0.7309
A3	1.618 (1.182, 2.054)	0.04033 (0.002893, 0.07776)	0.748
B1	3.043 (2.236, 3.85)	0.1474 (0.1095, 0.1853)	0.8166
B2	2.722 (2.203, 3.24)	0.004396 (−0.02377, 0.03256)	0.7824
B3	2.96 (−0.4771, 6.398)	0.1956 (0.07973, 0.3114)	0.3652
B2	2.722 (2.203, 3.24)	0.004396 (−0.02377, 0.03256)	0.7824

Table 6. Rate parameters for a two defects one and two photon annealing (M_1 + 2). In parenthesis the 95% confidence interval. Fit with Eq. (21)

M_1 + 2	b_1 (1/min)	b_2 (1/min)	R^2
A1	3.29 (2.698, 3.883)	0.1224 (0.1046, 0.1402)	0.9393
A2	1.854 (1.294, 2.414)	0.0462 (0.005655, 0.08675)	0.7308
A3	1.24 (1.107, 1.373)	0.0177 (−0.00163, 0.03704)	0.9589
B1	3.226 (2.458, 3.993)	0.2042 (0.1517, 0.2568)	0.883
B2	2.714 (2.49, 2.939)	0.004942 (−0.007094, 0.01698)	0.9714
B3	3.015 (−0.8869, 6.917)	0.2523 (0.0388, 0.4657)	0.365

Table 7. Rate parameters for a two defects with two photon annealing (M_2 + 2). In parenthesis the 95% confidence interval. Fit with Eq. (22)

M_2 + 2	b_1 (1/min)	b_2 (1/min)	R^2
A1	0.09564 (0.076, 0.1153)	4.358 (3.367, 5.35)	0.9397
A2	0.09272 (0.05091, 0.1345)	9.481 (5.127, 13.83)	0.7325
A3	0.01172 (−0.004615, 0.02805)	2.011 (1.817, 2.205)	0.9803

From the results the mechanism M_2 + 2 is ruled out because the rate coefficients b_1 and b_2 do not scale as the square of the intensity as expected for a two photon process. For M_1 + 1 the fits correspond to a slow and a fast process. The fast process coincides, within the uncertainties of the fit, with the one photon process in mechanism M_1 + 2.

The rate parameters depend on the intensity, not the power, and the set of measurements labeled A used a pump beam area twice as large as the set labeled B. Hence for the test of consistency with pump power a new parameter k was used defined as the rate coefficient was multiplied by the beam area for one photon processes (k = b*area) and by the beam area squared for two photon processes (k = b*area^2). The retrieved parameters were plotted as a function of pump power for M1 + 1 case and fitted with a linear function intercepting the origin (Fig. 10). For the M1 + 2 process the k1 parameter was plotted as a function of the power and k2 as a function of the power squared (Fig. 11). The R^2 of the fits were acceptable within the uncertainties of the measurement for the M_1 + 2 process and the linear correlation was found to be too poor for the M_1 + 1 process.

Optics EXPRESS

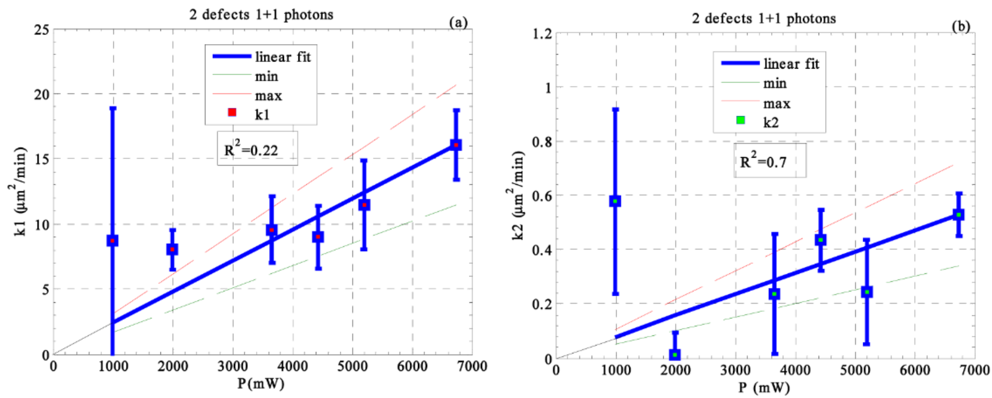

Fig. 10. Rate coefficients as a function of the pump power for the two defects, one and one photon annealing mechanism (M_1 + 1). a) k1 = beam area*b1 for the fast one photon contribution and linear fit (dashed lines indicate the confidence bounds from the linear fit). b) k2 = (beam area)*b2 for the slow one photon contribution and linear fit (dashed lines indicate the confidence bounds from the linear fit).

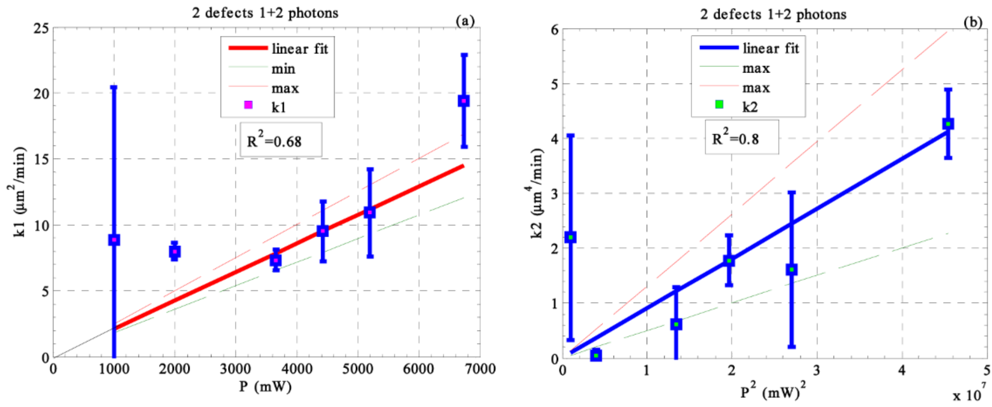

Fig. 11. Rate coefficients as a function of the pump power for the two defects, one and two photon annealing mechanism (M_1 + 2). a) k1 = beam area*b1 for the one photon contribution and linear fit (dashed lines indicate the confidence bounds from the linear fit). b) k2 = (beam area)^2*b2 for the two photon contribution and linear fit (dashed lines indicate the confidence bounds from the linear fit).

5. Conclusions

It has been found that defects in dielectric thin films responsible for the residual absorption are annealed under 1064 nm laser beam illumination with an intensity of up to 0.23 GW/cm^2. Changes in the absorptance of less than 10 ppm were detected using a photothermal microscope based on a focus error signal.

Several models were developed to analyze possible annealing mechanisms, that included stretched exponential relaxation, multiphoton processes and combinations of such processes including one defect type and two mechanisms (one and two photon absorption) which includes free carrier absorption, and two type of defects that annealed independently by one or two photon absorption. The choice of the most probable process was made by the consistency of the retrieved parameters with the expected dependence with the pump intensity. This analysis showed that the most probable mechanism responsible for the annealing is one in which two type of defects are present that anneal independently one by a one photon process and the other one by a two photon process. There are a family of shallow defects within the bandgap of amorphous oxides. In the case of amorphous SiO_2, energy

states 1-2 eV below the conduction band are associated with positively charged defects such as O_3^+ or Si_3^+ [1]. Non-bridging oxygen (O_1^-) are identified as acceptor states with binding energies of ~2 eV [1]. As one of the processes ruled out is the heating of the material by free carrier absorption, the temperature driven annealing predicted by full atomistic simulations of the annealing of amorphous SiO_2 [19] has been discarded. The passivation of the defects and reduction of the absorptance can be attributed to the trapping of the electrons in deep states, leaving the shallow states unoccupied as suggested in [12]. The fact that the shallow defects are not completely passivated by this mechanism might be explained in this model by the fact that not enough unoccupied deep traps are available.

Funding

DOD-USAF-Air Force (FA9550-13-1-0201); Universidad de Buenos Aires (UBACYT #20020170100137BA and PICT2015-1523).

References

1. E. P. O'Reilly and J. Robertson, "Theory of defects in vitreous silicon dioxide," Phys. Rev. B Condens. Matter **27**(6), 3780–3795 (1983).
2. A. S. Foster, F. Lopez Gejo, A. L. Shluger, and R. M. Nieminen, "Vacancy and interstitial defects in hafnia," Phys. Rev. B Condens. Matter Mater. Phys. **65**(17), 174117 (2002).
3. A. S. Markosyan, R. Route, M. M. Fejer, D. Patel, and C. Menoni, "Study of spontaneous and induced absorption in amorphous Ta2O5 and SiO2 dielectric thin films," J. Appl. Phys. **113**(13), 133104 (2013).
4. P. F. Langston, E. Krous, D. Schiltz, D. Patel, L. Emmert, A. Markosyan, B. Reagan, K. Wernsing, Y. Xu, Z. Sun, R. Route, M. M. Fejer, J. J. Rocca, W. Rudolph, and C. S. Menoni, "Point defects in Sc2O3 thin films by ion beam sputtering," Appl. Opt. **53**(4), A276–A280 (2014).
5. C. Xu, D. Li, H. Fan, J. Deng, J. Qi, P. Yi, and Y. Qiang, "Effect of different post-treatment methods on optical properties, absorption and nanosecond laser-induced damage threshold of Ta2O5 films," Thin Solid Films **580**, 12–20 (2015).
6. C. R. Wolfe, M. R. Kozlowski, J. H. Campbell, F. Rainer, A. J. Morgan, and R. P. Gonzales, "Laser Conditioning of Optical Thin Films" NIST Special Publication 801, Laser Induced Damage in Optical Materials: 1989, p. 360–375 (1990)
7. M. R. Kozlowski, C. R. Wolfe, M. C. Staggs, and J. H. Campbell, "Large Area Laser Conditioning of Dielectric Thin Film Mirrors" NIST Special Publication 801, Laser Induced Damage in Optical Materials: 1989 p. 376–392 (1990).
8. E. A. Domené, D. Schiltz, D. Patel, T. Day, E. Jankowska, O. E. Martínez, J. J. Rocca, and C. S. Menoni, "Thin film absorption characterization by focus error thermal lensing," Rev. Sci. Instrum. **88**(12), 123104 (2017).
9. E. A. Domené and O. E. Martínez, "Note: Focus error detection device for thermal expansion-recovery microscopy (ThERM)," Rev. Sci. Instrum. **84**(1), 016104 (2013).
10. O. E. Martínez, F. Balzarotti, and N. Mingolo, "Thermoreflectance and photodeflection combined for microscopic characterization of metallic surfaces," Appl. Phys. B **90**(1), 69–77 (2008).
11. C. S. Menoni, E. M. Krous, D. Patel, P. Langston, J. Tollerud, D. N. Nguyen, L. A. Emmert, A. Markosyan, R. Route, M. Fejer, and W. Rudolph, "Advances in ion beam sputtered Sc2O3 for optical interference coatings," Proc. SPIE **7842**, 784202.
12. S. Papernov, A. A. Kozlov, J. B. Oliver, T. J. Kessler, A. Shvydky, and B. Marozas, "Near-ultraviolet absorption annealing in hafnium oxide thin films subjected to continuous-wave laser radiation," Opt. Eng. **53**(12), 122504 (2014).
13. R. Kohlrausch, "Theorie des elektrischen rckstandes in der leidener asche," Ann. Phys. **167**(2), 179–214 (1854).
14. R. A. B. Devine, "On the physical models of annealing of radiation induced defects in amorphous SiO2," Nucl. Instrum. Methods Phys. Res. **46**(1-4), 261–264 (1990).
15. J. C. Phillips, "Microscopic aspects of Stretched Exponential Relaxation (SER) in homogeneous molecular and network glasses and polymers," J. Non-Cryst. Solids **357**(22-23), 3853–3865 (2011).
16. J. C. Phillips, "Stretched exponential relaxation in molecular and electronic glasses," Rep. Prog. Phys. **59**(9), 1133–1207 (1996).
17. J. C. Phillips, "Slow dynamics in glasses: A comparison between theory and experiment," Phys. Rev. B **73**(10), 104206 (2006).
18. S. C. Jones, P. Braunlich, R. T. Casper, X.-A. Shen, and P. Kelly, "Recent progress on laser- induced modifications and intrinsic bulk damage of wide -gap optical materials," Opt. Eng. **28**(10), 1039–1068 (1989).
19. F. V. Grigoriev, E. V. Katkova, A. V. Sulimov, V. B. Sulimov, and A. V. Tikhonravov, "Annealing of deposited SiO2 thin films: full atomistic simulation results," Opt. Mater. Express **6**(12), 3960 (2016).

181.170.142.48 {ts '2019-02-15 07:34:13'}